International Journal of GEOMATE
(Geotechnique, Construction Materials and Environment)
ISSN: 2186-2982 (P), 2186-2990 (O), Japan

Vol. 31, Issue 143, July, 2026, pp.155-171; DOI: 10.21660/2026.143.5456

FLEXURAL BEHAVIOUR OF STEEL FIBER REINFORCED CONCRETE SLABS ON GRADE

* Phuc Tran-Van [1]

[1] University of Architecture Ho Chi Minh City, Ho Chi Minh City, Vietnam

*Corresponding Author, Received: 26 Jan. 2026, Revised: 03 June 2026, Accepted: 04 June 2026

ABSTRACT: This study deals with the structural characteristics of steel fibre reinforced concrete (SFRC) slabs on grade without using traditional steel reinforcement mesh under static flexural loading. The experimental program was carried out on seven slabs (2000×1500×120 mm), including six SFRC slabs with steel fibre dosages varying from 10 to 40 kg/m^3 and one control conventional reinforced concrete (RC) slab. The slabs were supported by a spring system representing the elastic foundation, and a four-point loading scenario was used to investigate the response of the slabs under vehicle static loading. Experimental results of the slabs on grade demonstrated that SFRC slabs reduced the maximum relative displacement by 74–78 % and increased the service load limit (by up to 53 % compared with the RC slab. However, service loads reached 94 % of ultimate load in SFRC versus only 56 % in RC, indicating very limited reserve capacity. At the ultimate limit state, SFRC slabs exhibited 9–30 % lower ultimate loads and markedly lower ductility than the RC slab. Crack widths at failure were 76–85 % smaller in SFRC slabs than in RC slab. The results demonstrate that steel fibres can effectively replace mesh for serviceability performance, with 30 kg/m^3 being the practical optimum dosage.

Keywords: Steel fibre reinforced concrete (SFRC); Slab on grade; Flexural strength; Ultimate limit state.

1. INTRODUCTION

Conventional concrete slabs on grade in industrial buildings are well-known for their inherent weakness in resisting crack development during construction or shortly after being put into use. The primary reasons for this unfavorable failure are attributed to the small tensile strength and shrinkage of concrete. In addition, the impact of dynamic loads induced by the movement of the equipment and motor vehicles contributes to the generation of localized stresses on the concrete slabs, which tend to widen the cracks in the structures and induce sudden brittle failures. Consequently, the service life and durability of the structures are degraded. Recently, the solution of adding steel fibers as reinforcements to concrete (known as steel fiber reinforced concrete - SFRC) has been widely adopted in slab-on-grade construction due to its ability to control cracks, prevent shrinkage, and improve the ductility and performance of the structures [1–6]. In addition, SFRC not only exhibits excellent resistance to wear actions, fatigue, and impact loads [7–9] but also effectively enhances flexural strength [10–15] and shear resistance [16–20] of concrete structures. From the construction perspective, dispersed fibers are suitable for various types of structures thanks to their small sizes, especially for slab-type structures with limited cross-sectional height [21–24]. Several studies have been devoted to investigating the effects of steel and synthetic fibers on the cracking behavior of slab-on-grade structures [10,25–28]. These previous studies indicated that both steel and synthetic fibers effectively control cracking and significantly improve the crack resistance of the slabs, particularly in the early stages. Other studies about the effect on concrete slabs on grade [29–33] also confirmed that using steel fibers and synthetic fibers provides an economically efficient design of the slabs, where the fibers considerably improve the flexural strength of the slabs.

Although the aforementioned studies both agreed that fibers significantly affect the structural behavior of slabs on grade, the effects of fiber dosage, especially steel fibers, on the improvements of crack-control and load-bearing characteristics of SFRC slabs on grade have not been fully and systematically investigated. It is worth mentioning that most of the previous studies about SFRC slabs on grade focus on clarifying the efficiency of the SFRC slabs on grade by comparing the structural performance of the fiber-reinforced slabs to that of the plain concrete slabs. In practice, concrete slabs on grade are often reinforced with steel meshes to control cracking and ensure the structural integrity of the structure [34], which is important for the normal operation of buildings and the safety of users. Since the behavior and failure modes of plain concrete slabs and RC slabs are different [16,35,36], distinguishing the performance of fiber-reinforced slabs from that of plain concrete slabs highlights the effect of fibers but does not fully demonstrate the superior performance of fiber-reinforced slabs compared to conventional RC slabs. This fact shows that further experimental studies are really necessary to provide a more reasonable evaluation of the effect of fiber dosage on the structural characteristics of the SFRC slabs on grade and thorough clarifications of their efficiency in comparison with the conventional RC slabs.

Although several previous studies have investigated the effects of steel and synthetic fibers on the cracking behaviour and flexural performance of slabs on grade, the majority compared SFRC slabs only with plain concrete slabs rather than with conventionally RC slabs containing steel mesh, which is the standard practice for controlling cracking and ensuring structural integrity in industrial floors and slabs on grade. In addition, most experimental investigations employed either full-scale field tests with patch or uniform loading or small-scale specimens under simplified support conditions, with very limited data available for scaled slabs tested under realistic multi-wheel contact loading on precisely calibrated elastic foundations. To the best of the authors' knowledge, this study is the first to experimentally investigate the flexural behaviour of 1:2 scaled SFRC slabs on grade (2000×1500×120 mm) supported on a calibrated Winkler spring system (k = 1840 kN/m³) and subjected to a four-point wheel-contact loading configuration that simulates actual vehicle tyre pressures. Steel fiber dosages were systematically varied from 10 to 40 kg/m³, with the maximum dosage deliberately chosen to match the equivalent steel weight provided by the Ø6@200 mm mesh used in the control RC specimen. Complementary tests on eighteen notched beams were also performed to obtain residual tensile strengths of SFRC concrete. In relatively thin slabs (120 mm thick), steel fibers tend to align preferentially in the horizontal plane during vibration and casting, resulting in a predominantly two-dimensional orientation rather than the ideal three-dimensional random distribution. This reduces the number of fibers effectively crossing vertical crack planes and may lower the effective bridging efficiency compared with theoretical assumptions. Scale effects also represent a notable limitation in laboratory testing. Although the slab thickness was kept at the full-scale value (120 mm) to maintain realistic fiber distribution and flexural stiffness, the 1:2 in-plane geometric scaling may still introduce minor differences in crack spacing, fracture energy, and overall structural response when extrapolating results to prototype structures. In addition, the present study has several other limitations, including the simulation of continuous soil support by a discrete Winkler spring system, the relatively low compressive strength of the concrete matrix, the use of only monotonic static loading (no fatigue or repeated loading), and the testing of only one specimen per fiber dosage due to the large scale and high cost of the experiments. These aspects are acknowledged and discussed further in the experimental programme and results sections. Therefore, this work addresses the identified knowledge gap by providing the first direct and systematic comparison of SFRC performance with conventional RC mesh practice under realistic wheel loading and foundation conditions.

2. RESEARCH SIGNIFICANCE

This study experimentally investigates the structural behaviour of SFRC slabs on grade under realistic vehicle wheel loading conditions. Unlike most previous studies that mainly compared SFRC slabs with plain concrete slabs, this study evaluates SFRC slabs against a conventional RC slab with an equivalent reinforcement ratio. A calibrated Winkler spring system and a four-point wheel-contact loading configuration were adopted to simulate slab-soil interaction and vehicle loading. The results improve understanding of the effects of steel fiber dosage on crack control, stiffness, serviceability, and ultimate behaviour of thin SFRC slabs on grade.

3. EXPERIMENTAL PROGRAM

3.1 Materials properties and influence of steel fiber contents on residual flexural tensile strength

The concrete mix design was designed as follows: PC40 cement (344 kg/m³), coarse aggregate (22-25 mm, 1308 kg/m³), fine aggregate (1-4 mm, 639 kg/m³), water (195 liters/m³), and plasticizer (4.2 liters/m³). Dramix 3D 65/35 BG steel fibers (Bekaert) were used in this study with different dosages to generate seven concrete mixtures, namely 0, 10, 15, 20, 25, 30, and 40 kg/m³. The fibers are hooked-end Dramix 3D 65/35 BG steel fibers with a nominal diameter and length of 0.55 mm and 35 mm, respectively. The elastic modulus of steel fibers is E_{sf} = 210000 MPa, their nominal tensile strength $R_{n,nom}$ = 1345 MPa, and the number of steel fibers per unit weight is 14531 fibers/kg. The concrete mixtures had a slump of 120±20 mm achieved in all batches and it was proportioned with a target water-to-cement (w/c) ratio of 0.57. The actual *w/c* ratio was 195 kg water per 344 kg cement = 0.567. The plasticizer was used as the plasticizer at a dosage of 4.2 *L/m³*. No air-entraining admixture was incorporated, and the fresh air content was not measured during mixing and casting. It is worth noting that the mixture of the aforementioned concrete matrix was intentionally designed to match the actual design strength used for road slabs in the countryside. The concrete mixtures were prepared in a laboratory pan mixer following a controlled sequence to ensure good fiber dispersion: (1) dry mixing of cement, coarse aggregate (22–25 mm) and fine aggregate (1–4 mm) for 2 min; (2) addition of approximately 70 % of the mixing water together with the polycarboxylate-ether-based high-range water reducer (4.2 L/m³ by volume of concrete) and mixing for 3 min; (3) gradual addition of the remaining water; and (4) slow, continuous introduction of the Dramix 3D 65/35 BG hooked-end steel fibers over a 2–3 min period while the mixer operated at high speed, followed by an additional 4–5 min of mixing. Fibers were added in small batches to prevent balling. Visual inspection of the fresh mix showed uniform fiber distribution with no noticeable balling up to 30 kg/m³. At the highest dosage of 40 kg/m³, minor fiber balling and local clustering were occasionally observed during mixing, which is considered the primary cause of the slight reduction in compressive and flexural strength recorded for mixture C40 (see Table 1). Post-hardening visual examination of sawn cross-sections from selected beam and slab specimens confirmed reasonably uniform fiber orientation and distribution for dosages ≤ 30 kg/m³; some localised clustering was noted at 40 kg/m³. No quantitative fiber counting in sections was performed in this study. To determine the cubic compressive strength (f_{cu}) of the concrete, average results of five 150×150×150 mm cube samples were tested following TCVN 10303:2014 [37] and TCVN 8862:2011 [38]. The flexural tensile strength ($f_{t,fl}$) was determined on three 150×150×500 mm beam samples following ASTM C1609:2019 [39]. To determine the residual tensile strength of SFRC, the notched beam samples were designed according to EN-14651 [40] and RILEM TC 162-TDF [41] as shown in Fig. 1, where the depth and the width of the notch are 25 mm and 3 mm, respectively. It is noted that the cross-section labelled as “Fracture area” in Fig. 1 does not represent the actual irregular fractured surface after testing. It shows the nominal notched ligament cross-section (the remaining concrete section above the notch) that is deliberately used for calculating the residual flexural tensile strengths fRi according to RILEM TC 162-TDF [41]. These notched beams had varying steel fiber dosages (m_f) of 0, 10, 15, 20, 25, 30, and 40 kg/m³, respectively, and were made with the same concrete batches of the corresponding slabs. It is worth noting that the concrete mix used in this study was intentionally designed with relatively low compressive strength (f_{cu} ranging from 20.75 MPa to 31.95 MPa) to replicate the actual concrete grade commonly employed for road slabs and industrial floors in rural areas of Vietnam, where economic constraints and local construction practices typically limit the use of high-strength concrete. This choice also provided a more critical test condition for evaluating steel fiber performance, as lower matrix strength generally results in weaker fiber–matrix bond, particularly at higher fiber dosages. The steel bars used to make the steel meshes in the control slab specimen (Ø6 plain bars) had a yield strength (f_y) of 395 MPa and an ultimate strength (f_u) of 528 MPa. Those values were determined as an average of three samples according to TCVN 197-1:2014 [42].

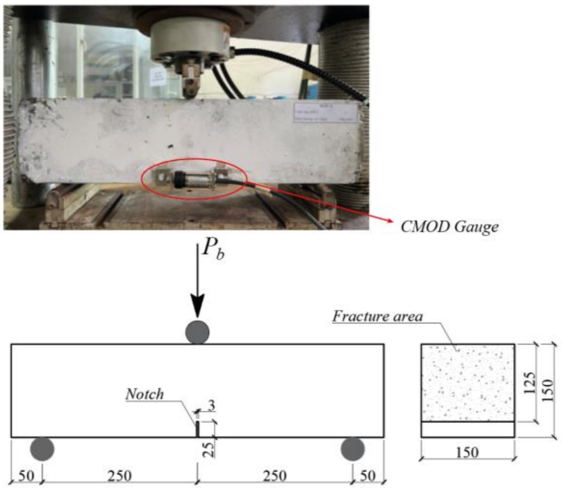

Fig. 1 Dramix 3D 65/35 BG steel fibers and three-point bending test setup based on RILEM TC 162-TDF [41]

The compressive strength and flexural strength taken as mean values in material tests are presented in Table 1. It is noted that there was a reference mixture (C0) without any steel fibers, and this concrete mixture was used to prepare a control slab specimen with conventional steel mesh. As illustrated in Fig. 2a, the increase of steel fiber dosage up to 30 kg/m^3 witnessed elevations of compressive strength and flexural tensile strength of SFRC concrete, while the use of a higher steel fiber dosage of 40 kg/m^3 led to slight decreases of concrete strength. The addition of steel fibers has been well documented to enhance the compressive strength of SFRC due to the effects of delaying the lateral expansion and restraining the crack propagation under compressive load [43,44]. Similarly, the increase in flexural tensile strength was attributed to the increase in the number of steel fibers in the tensile zone of the specimen [44]. The noticeable reduction of concrete strength when a steel fiber dosage of 40 kg/m^3 in this study could be attributed to the fact that the strength of the conventional concrete matrix (C0 mixture with coarse aggregate sizes ranging from 22-25 mm) was relatively low, leading to adversely effect in bond strength between steel fibers and concrete matrix when a considerable steel fiber dosage is used [43]. This effect is reasonable as the degree of increase in concrete compressive strength became smaller with larger steel fiber dosages being used, as illustrated in Fig. 2a. In addition, the mixing and placing procedures of small quantities of concrete used to prepare the small-size specimens in this study might contribute to uneven dispersion of steel fibers.

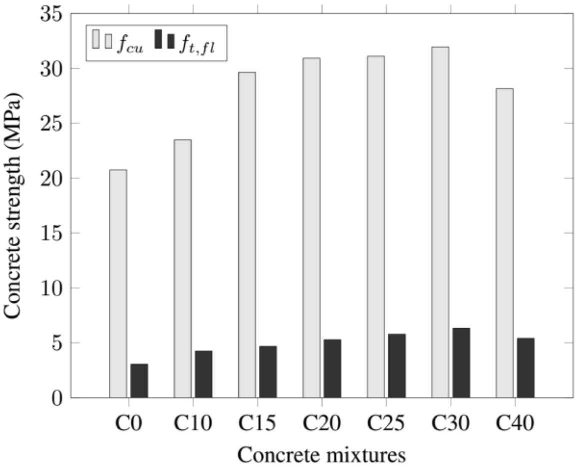

a. Compressive strength (f_{cu}) and flexural tensile strength ($f_{t,fl}$)

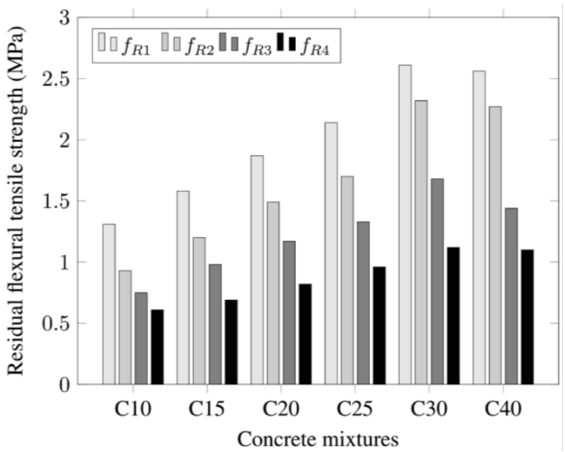

b. Residual flexural tensile strength f_{Ri}

Fig. 2 Effects of steel fiber dosages on properties of SFRC concrete

The average P_b-CMOD (load versus crack mouth opening displacement) relationships and the residual flexural tensile strength collected from 21 notched beam samples (three for each concrete batch) with varying steel fiber dosages of 0, 10, 15, 20, 25, 30, and 40 kg/m³ are illustrated in Fig. 3 and Fig. 2b. It is noted that the residual flexural tensile strengths (f_{R1}, f_{R1}, f_{R1}, and f_{R4}), which are used to represent the ability of SFRC to resist tensile and flexural stresses after cracking, are determined from the loads at CMOD1 = 0.5 mm, CMOD2 = 1.5 mm, CMOD3 = 2.5 mm, and CMOD4 = 3.5 mm, respectively, as per RILEM TC 162-TDF [41]. In general, the softening-strain responses were captured in all specimens. Additionally, the conditions that the SFRC could substitute (also partially) conventional reinforcement at the ultimate limit state according to *fib* model code [45] were all fulfilled based on the averaged results of flexural residual strength, i.e., $f_{R1}/f_L > 0.4$, $f_{R3}/f_{R1} > 0.5$.

Table 1. Compressive strength and flexural tensile strength of concrete (Standard deviations are presented in brackets)

Mixture	ρ_s (kg/m^3)	V_f (%)	f_{cu} (N/mm^2)	$f_{t,fl}$ (N/mm^2)	f_L (MPa)	f_{R1} (MPa)	f_{R2} (MPa)	f_{R3} (MPa)	f_{R4} (MPa)
C0	0	0	20.75(1.19)	3.05(0.12)	1.97(0.08)	-	-	-	-
C10	10	0.13	23.48(1.22)	4.24(0.16)	2.26(0.08)	1.31(0.07)	0.93(0.06)	0.75(0.08)	0.61(0.05)
C15	15	0.19	29.64(1.54)	4.67(0.13)	2.50(0.07)	1.58(0.06)	1.20(0.07)	0.98(0.08)	0.69(0.06)
C20	20	0.25	30.93(1.59)	5.28(0.21)	2.87(0.08)	1.87(0.07)	1.49(0.07)	1.17(0.07)	0.82(0.09)
C25	25	0.32	31.10(1.47)	5.78(0.24)	3.18(0.06)	2.14(0.08)	1.70(0.05)	1.33(0.06)	0.96(0.08)
C30	30	0.38	31.95(1.55)	6.33(0.27)	3.38(0.10)	2.61(0.07)	2.32(0.04)	1.68(0.08)	1.12(0.08)
C40	40	0.50	28.15(1.36)	5.39(0.20)	2.88(0.08)	2.56(0.07)	2.27(0.07)	1.44(0.05)	1.10(0.07)

Notes: ρ_s is steel fiber dosage; $V_f = \rho_s \times 100/7850$ is the volume fraction of steel fibers, f_{cu} is the cubic compressive strength of concrete, $f_{t,fl}$ is the flexural tensile strength, f_L and f_{Ri} are the proportional limit and residual flexural tensile strength obtained from the notched beam test.

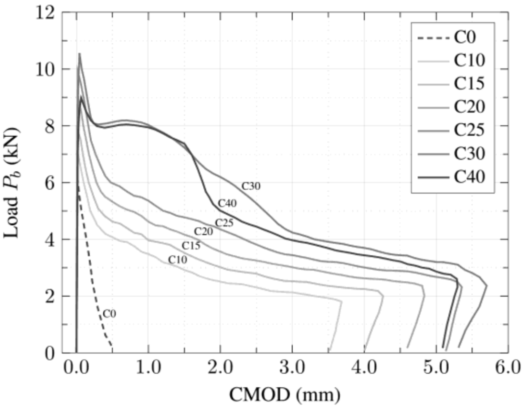

Fig. 3 P_b-CMOD relationships from bending tests

Similar to the tests for compressive strength and flexural tensile strength, the residual flexural tensile strengths fRi increased substantially with the rise of steel fiber dosages up to 30 kg/m³, while slight decreases are observed in the specimens with steel fiber dosage of 40 kg/m³, presumably due to the reduction of bonding strength between the concrete matrix and steel fibers. Compared to f_{R2} and f_{R3}, the increase in flexural residual tensile strength f_{R1} is less noticeable. This phenomenon could be attributed to the fact that f_{R1} is determined at a small CMOD value (0.5 mm). At this stage of tensile deformation with a narrow crack width, the contribution of steel fibers is less noticeable as the strength of steel fibers is not effectively exploited yet. The residual flexural tensile strength f_{R4} increased gradually with the increase of steel fiber dosage. In fact, f_{R4} was determined at a load level corresponding to a very large CMOD (3.5 mm). At this load level, the crack width of the concrete sample is large, and the sample has reached the failure state, which can reduce the efficiency of the bridging mechanism of the steel fibers. As a result, the increase of f_{R4} with the elevation of steel fiber dosage is less pronounced as observed in the cases of f_{R1}, f_{R2}, and f_{R3}. Overall, the results obtained from the bending tests indicated that the effect of steel fiber dosage on improving residual flexural tensile strength f_R varies according to the CMOD or crack width. In addition, the impact of steel fiber dosage is most evident in the CMOD range of 1.5 to 2.5 mm.

3.2 Slab specimens and subgrade preparation

The testing slabs in this study are assumed to rest on natural soil foundations. From the initial design, a segment of the concrete slab has dimensions of 4000×3000×120 mm (length×width×thickness) according to practical considerations. Due to the difficulties of testing on large-scale structures, the experimental program was conducted on seven specimens at a scale of 1:2 compared to the actual size of the design for concrete slabs, as mentioned previously. All specimens have dimensions of 2000×1500×120 mm as depicted in Fig. 4. It is worth noting that the experimental program employed a 1:2 scaled model relative to the prototype slab (4000×3000×120 mm). Geometric similarity was applied in plan (length and width scaled by 2) while slab thickness was kept at the prototype value h = 120 mm (scaled model). This is standard practice for slab-on-grade testing because the actual slab thickness governs fiber distribution, crack spacing, and flexural stiffness; scaling thickness would distort these phenomena unrealistically. Material similarity was maintained (identical concrete matrix, steel fibers, and mesh). Load similarity followed a gravity-dominated structure and can be calculated accordingly for full-scale slab-on-grade systems. Stiffness similarity for the foundation was achieved by using the same subgrade modulus k = 1840 kN/m³ in the model (no scaling applied to k because soil stiffness is independent of geometric scale when the same soil type is simulated).

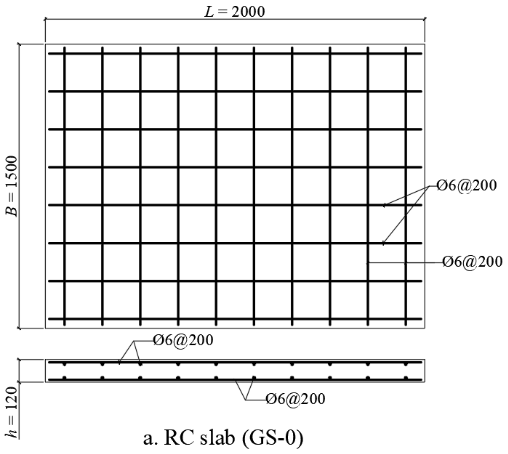

a. RC slab (GS-0)

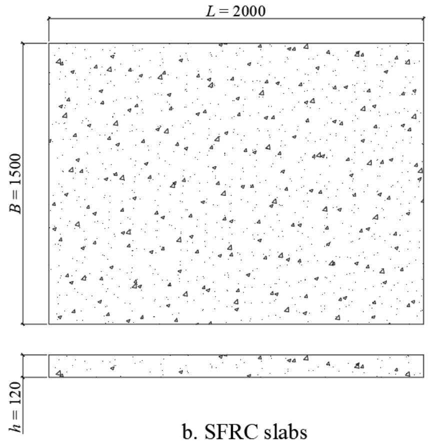

b. SFRC slabs
(GS-10, GS-15, GS-20, GS-25, GS-30, GS-40)

Fig. 4 Details of slab specimens

The experimental program includes one control specimen (GS-0), which was reinforced with two layers of welded wire mesh fabricated from Ø6 mm plain bars spaced at 200 mm centres in both longitudinal and transverse directions (Ø6@200 mm). One mesh layer was placed near the top surface and the other near the bottom surface, with a nominal clear cover of 20 mm to the outermost bars at both top and bottom faces. This resulted in symmetric placement about the mid-depth of the 120 mm thick slab. The cross-sectional area of steel provided by each mesh layer per metre width is 141.4 mm²/m. With two layers, the total steel area is 282.7 mm²/m. The reinforcement ratio based on the gross concrete section (b = 1000 mm, h = 120 mm) is ρ = 0.236%. The remaining specimens are six SFRC slabs (GS-10, GS-15, GS-20, GS-25, GS-30, and GS-40) with corresponding steel fiber dosage of 10, 15, 20, 25, 30, and 40 kg/m³. The maximum steel fiber dosage (40 kg/m³) in SFRC slabs was deliberately designed to match the weight of the Ø6 steel meshes in the control slab for comparison purposes. It is worth noting that the steel meshes Ø6@200mm only provided a steel reinforcement ratio smaller than the minimum requirement in design practice. These testing slabs were cast simultaneously in an area having a temperature of approximately 30°C and a measured humidity of around 75%. The concrete was compacted using a hand-held concrete vibrator to ensure uniformity and eliminate air bubbles. After casting, the top surface of the slabs was levelled and immediately covered to prevent moisture evaporation. The specimens were demoulded at an age of 24 hours. Wet curing was continued by keeping the slabs continuously moist (using wet burlap and periodic water spraying) for 7 days. All slab specimens together with the companion material samples were tested at the age of 28 days.

The structural response of the foundation was simulated using a Winkler spring system, in which the subgrade modulus was chosen to be equivalent to the actual stiffness of the soil foundation layers in the countryside regions having extremely soft subgrade. The springs were fabricated by adopting steel wire having a diameter of d = 16 mm, the outer diameter of the springs is D = 120 mm, and the height is h = 200 mm as presented in Fig. 5. Spring stiffness was determined experimentally. It is noted that the subgrade modulus k = 1840 kN/m³ was selected to represent the extremely soft rural soil conditions in Vietnamese countryside regions (typical range for soft clay 1–5 MN/m³), and the average measured stiffness per spring was used to derive the equivalent subgrade modulus by dividing spring stiffness by the tributary area of each spring.

Fig. 5 Detail of a spring and stiffness test

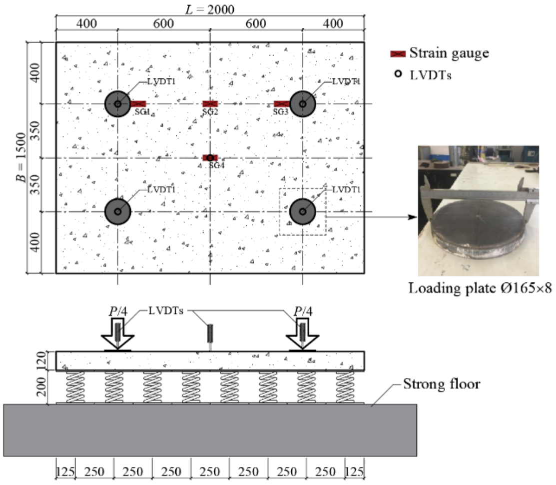

a. Plan view and side view of experimental setup, loading configuration, and arrangement of strain gauge and LVDTs

b. Slab placement and loading procedure

Fig. 6 Experimental setup

To secure the springs to the concrete slabs and reaction floor, two end caps were also fabricated from square steel plates and steel piles. The square steel plates were 250 mm in width and 8 mm in thickness, while the steel pipes' wall thickness×diameter×height were 4×88×50 mm, respectively. After the springs were completely fabricated, they were tested to determine their actual stiffness (Fig. 5). The tested results showed that the average equivalent stiffness of the spring system was 1840 kN/m³. After calibrating the position of the spring system, the slab specimens were laid onto the spring foundation system as depicted in Fig. 6. Discrete springs approximate continuous soil support when grid density is high (spacing < slab thickness); however, they cannot capture lateral shear interaction or continuity between soil elements. The discrete-spring approximation is acceptable for preliminary design but slightly overestimates local deflections compared with a continuous elastic half-space. Furthermore, the spring model neglects soil shear stiffness, Poisson’s ratio effects, and nonlinear soil behavior at high loads. It is suitable for serviceability assessment but may underestimate load redistribution in highly cracked states; more advanced Pasternak or continuum models would be required for ultimate-limit-state precision. These limitations are acknowledged and do not affect the comparative conclusions between SFRC and RC slab.

3.3 Experimental setup and loading protocol

Illustration of the experimental setup and arrangement of measurement devices are shown in Fig. 6. The hydraulic jack applied a load of *P* to a beam system (as shown in Fig. 6b), which then distributed the load into four vertically concentrated loads, *P*/4, onto four round steel plates simulating the contact surfaces of four wheels of a lightweight pickup truck as illustrated in Fig. 7. The compressive and tensile strains of the slabs were determined based on four strain gauges (SG) attached to the surfaces of the slabs as depicted in Fig. 6: SG2 and SG4 at mid-span positions on the bottom surface, SG1 and SG3 at two support points on the top surface. The locations of those SG were based on the assumed compressive regions of the structures. The displacement of the slab is measured using five linear variable differential transformers (LVDTs) placed at the mid-span and the four load application points.

The slabs were loaded under a load-controlled procedure with load increments being applied at a rate of 7 kN/min (≈ 0.12 kN/s). This rate was selected to ensure quasi-static loading that allows stable crack propagation, accurate visual observation, and reliable data acquisition without introducing dynamic or inertial effects. The chosen rate is consistent with standard practices for large-scale static slab tests reported in the literature for monotonic flexural testing of ground-supported slabs. At this slow loading rate, strain-rate effects on concrete compressive and tensile strength are negligible for normal-strength concrete, as dynamic increase factors become significant only above strain rates of 10^{-1} s^{-1}. No cyclic or repeated loading was applied; the test was purely monotonic until flexural failure. At each load increment, the applied load was held constant for approximately 3 minutes solely to allow manual crack-width measurement, photographic documentation, and stable recording of LVDT and strain-gauge readings. During these short hold periods, neither creep nor relaxation was significant, as evidenced by the near-constant load and displacement readings (variation < 1 %). Long-term creep effects were outside the scope of this short-duration static strength test. The slab specimens were tested under free-edge conditions. No edge beams, rotational restraints, tie-downs, or continuous line supports were provided along any of the four perimeter edges. Vertical support was furnished exclusively by the internal grid of helical springs (spacing 200–250 mm) that simulated the Winkler foundation. Each spring was connected to the slab soffit by a square steel end plate (250 × 250 × 8 mm) and a short steel pipe welded to the plate. These end plates were not bonded, anchored, or glued to the concrete; the slab simply rested on them under its self-weight. Consequently, only minor frictional resistance existed between the steel plates and the concrete bottom surface. No lateral (horizontal) restraints or friction-enhancing devices were installed along the edges. This configuration allowed free rotation and minor uplift at the perimeter while preventing gross vertical separation. The free-edge support conditions, combined with the four-point wheel-contact loading, produced the observed one-way slab behaviour and the formation of three parallel yield lines running perpendicular to the long edge of the slab. The hydraulic jack load (*P*) was applied at the centre of a stiff steel distributing beam with dimensions 2200 mm (length) × 200 mm (depth) × 150 mm (width), fabricated from a welded I-section. The flexural stiffness of the beam ($EI \approx 2.8 \times 10^{13}$ N·mm⁴) was sufficiently high to ensure negligible deformation and virtually uniform load distribution under the maximum applied load. The beam transferred the load through four vertical loading rods to four circular steel contact plates. Each contact plate had a diameter of 150 mm and thickness of 25 mm, resulting in contact stiffness far greater than that of the concrete slab. The plates were placed on a thin (5 mm) sand-cement mortar bed to achieve uniform pressure distribution and were mounted on spherical bearings, allowing free rotation to better simulate real tyre contact behaviour. The centre-to-centre spacing of the four contact plates was 900 mm in the longitudinal direction and 1200 mm in the transverse direction, replicating the wheel configuration of a typical lightweight pickup truck (see Fig. 7). Equal load distribution (*P*/4 at each plate) was assumed due to the symmetry of the setup and was verified in real time using individual load cells placed beneath each contact plate. The four-point loading configuration was designed to simulate typical wheel loads from light vehicles such as pickup trucks used on rural roads and industrial floors. Although the exact wheel spacing of any particular truck model was not replicated, the chosen spacing of 900 mm (longitudinal) × 1200 mm (transverse) produces realistic one-way slab flexural behaviour and the characteristic three parallel yield lines observed in practice. The circular steel plates (150 mm diameter) simulate tyre contact areas, and the resulting failure pattern matches field observations of slabs on grade under vehicle loading. The reference to a lightweight pickup truck in Fig. 7 is illustrative of the general class of vehicle rather than an exact geometric match. The experiments were terminated by the flexural failure of the specimens, which is characterized by an abrupt deformation of the structures and sudden growth of crack width. At the end of each load increment, the applied load was held for approximately three minutes to record the displacements, crack width, and compressive strains of concrete. All values for force, displacement, and strain were automatically recorded through a data acquisition system.

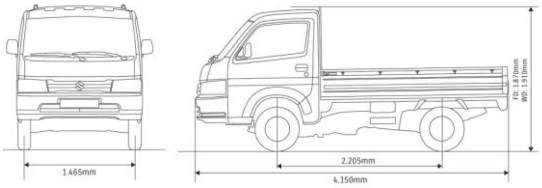

Fig. 7 Technical specifications of a lightweight pickup truck [49]

4. EXPERIMENTAL RESULTS AND DISCUSSION

4.1 Crack patterns and failure modes

Under the loading procedure where the vertical loads were applied simultaneously at four steel plates, all slab specimens moved downward as rigid body translations in the early stage of the tests. When the applied loads were increased to a certain value, visible cracks appeared first on the top surface of the slabs, then all the slabs began to bend in a convex profile with the apex line being located in the middle of the slab, parallel to the short edge of the slabs. Later, primary cracks emerged at the center of the top surface and subsequently at the loading regions, where cracks' mouths were seen mostly on the bottom surface. The failure of all slab specimens was indicated by the abrupt deformation of the structures and enlargement of the crack width, while no crushing failure was observed.

As presented in Fig. 8, the control RC specimen (GS-0) failed in flexure due to primary cracks running along the shorter edge at the loading points (supports) and mid-span. The failure mode of the GS-0 slab resembled the behaviour of a one-way slab under a uniform distributed load with the loading points acting as supports. At the failure, the concrete at the loading regions (under compression from the applied loads) was not crushed. In addition, most of the slabs (GS0, GS15, GS20, GS25, and GS30) were divided into four separate rigid segments, forming a failure mechanism with three parallel failure lines being developed at the center and loading regions of the slabs.

In Fig. 8 it is observed that the other SFRC slabs also failed in flexure due to primary cracks, mostly at mid-span (all slab specimens) and at two loading regions (GS-15, GS20, GS25, and GS30). The primary cracks observed in SFRC specimens ran along the short edge, and the slabs were split into separate rigid bodies at the failure state. Similar to the control RC slab, the failure mode of these SFRC slabs can also be depicted as an inverted slab under uniform distributed load acting in the upward direction, while the concrete beneath the loading plates was not crushed. It is noted that the failure modes of GS-10 and GS-40 specimens did not replicate the obvious failure of the other slabs, which formed three parallel yield lines along the short edge direction. The difference in failure mode in such specimens might be attributed to the uneven effect of SFRC in improving the flexural strength and crack resistance, and the difference between the loads at loading points due to the horizontal translations at the large deformation stage of the slabs during the experiments.

Scaling effects on cracking patterns, fiber distribution, flexural capacity, and ductility were minimal because thickness remained unchanged: fiber orientation statistics, bond length, and crack-width development are thickness-dependent and therefore identical to the prototype. Cracking patterns (parallel yield lines) are preserved due to the one-way slab behavior. Flexural capacity scales with area while stresses remain directly comparable. Ductility (measured as displacement ductility ratio $\mu = \delta_u/\delta_{ser}$) is also representative because the same concrete tensile mechanisms govern both scales. It it woth noting that Minor size effects on fracture energy may slightly underestimate crack spacing in larger prototypes; however, the 1:2 ratio and identical thickness minimize these issues compared with fully scaled models.

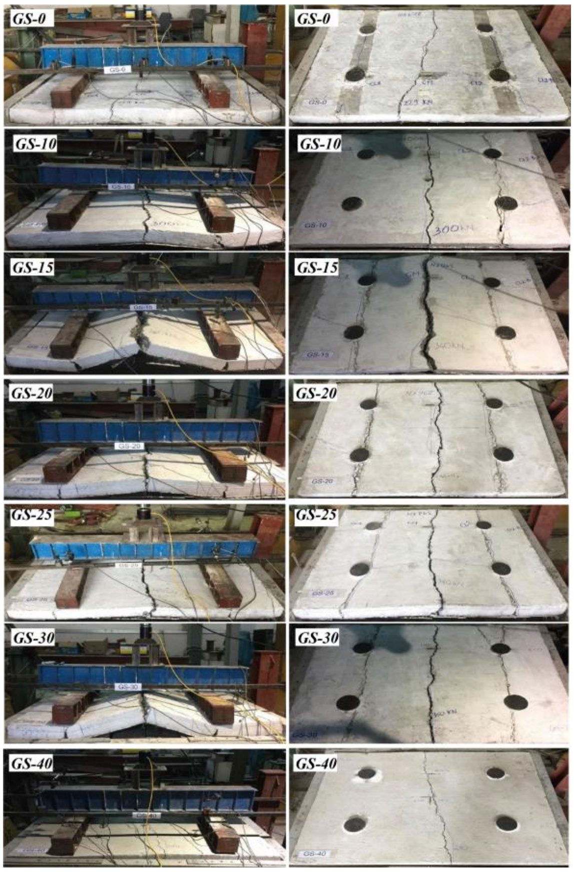

Fig. 8 Failure modes and crack patterns

4.2 Cracking and ultimate loads of slab specimens

The main results obtained from the experimental program of all slabs on grade are summarized in Table 2 and comparisons of different load levels and deformations at failure between slab specimens are presented in Fig. 9. It is seen that the cracking loads (P_{cr}: the load level at which the first critical cracks were captured) obtained from SFRC slabs were generally higher than that of the control RC slab. Specifically, the cracking loads of the SFRC slabs with fiber dosages of 10, 15, 20, 25, 30, and 40 kg/m³ (GS-10, GS-15, GS-20, GS-25, GS-30, and GS-40) increased by 28%, 41%, 44%, 46%, 55%, and 47%, respectively, compared to the control RC slab (GS-0). The elevation of cracking loads is consistent with the outcomes of flexural tensile strength obtained from material tests in Table 1, although the cracking loads of slabs with steel fiber dosage greater than 15 kg/m³ did not increase linearly with the rise of steel fiber dosage. This is understandable since the steel fibers only play their role in resisting tensile stress when the concrete cracks occur. The observation of cracking loads (P_{cr}) indicates that the effects of traditional steel reinforcements in improving the crack resistance of the control RC slab (GS-0) were not as efficient as those of SFRC slabs in the pre-cracking stage. The use of steel fibers in this study proved to be more beneficial than using reinforcement meshes placed on both the top and bottom surfaces of the slab to improve crack resistance.

Regarding the limit service loads (P_{ser}), the results presented in Fig. 9 show that the strength of SFRC slabs at service conditions is considerably greater than that of the control RC slab. It is noted that the service load in this study is defined as the load level at which the mid-span displacements are equal to the allowable displacement of concrete structures in the limit service state according to Eurocode 2 [46], where $\delta_{SLS} = l/250$, l = 1200 mm. Overall, the limit service loads of the SFRC slabs with fiber dosages of 10, 15, 20, 25, 30, and 40 kg/m³ were respectively 19%, 41%, 42%, 44%, 53%, and 46% higher than that of the control RC slab. In addition, the enhancement of service loads by using steel fiber dosage greater than 15 kg/m³ was not significantly different, as the width of the cracks at this stage was relatively small and the contribution of steel fibers was not fully exploited. The enhancement of cracking loads could be attributed to the effect of dispersed steel fibers, which effectively controlled and limited the development of cracks and reduced tensile stress in the concrete. As a result, the stiffness degradation was delayed, and significant improvements in the limit service loads were observed**.** The limit service loads of the SFRC slabs without traditional reinforcing steel bars were found to be close to their ultimate failure load (P_u), approximately 94% of P_u. In contrast, the P_{ser} of the control RC slab was only 56% of its ultimate load as shown in Table 2. On one hand, these results show the high efficiency of steel fibers in replacing traditional reinforcing steel bars for structures having small allowable deformations, like slabs on grade. On the other hand, fully replacing traditional steel bars with fibers for structures characterized by large deformations and allowing internal force redistribution requires careful consideration to ensure sufficient reserve capacity and structural safety. The substantial increase in service load limit (up to 53 %) of SFRC slabs compared with the control RC slab can be explained by two primary mechanisms. First, the pre-cracking stiffness of SFRC slabs was 12–45 % higher than that of the RC slab, as evidenced by the 12–45 % smaller displacements at the cracking load P_{cr}. This improvement results from the ability of dispersed steel fibers to effectively control micro-cracks caused by shrinkage and early tensile stresses, thereby maintaining a higher effective elastic modulus. Second, after initial cracking, fiber bridging across cracks significantly limited crack opening and slowed the rate of stiffness degradation (the slope of the load–displacement curve in the post-cracking phase was markedly lower for SFRC). Consequently, a substantially higher load was required for the SFRC slabs to reach the serviceability deflection limit ($\delta_{ser} = l/250$) compared with the RC control slab.

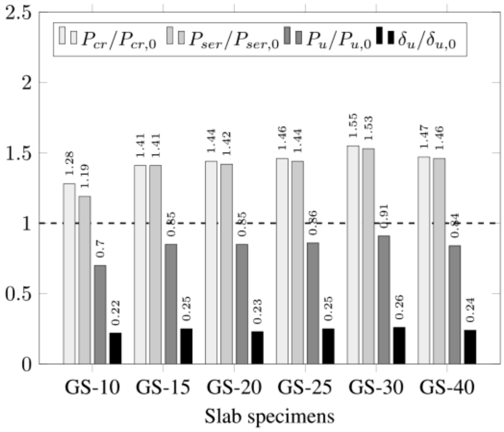

Fig. 9 Effects of steel fiber dosage on the behaviour of slabs on grade. (Notes: $P_{cr,0}$, $P_{ser,0}$, $P_{u,0}$, and $\delta_{u,0}$ are the crack load, service load, ultimate load, and relative displacement at the failure of the control RC slab GS-0)

It is acknowledged that only a single slab specimen was tested for each steel-fiber dosage (and the control RC slab). Given the large specimen size (2000×1500×120 mm) and the high cost of fabrication, instrumentation, and testing on a calibrated spring foundation system, replicate slabs per mixture were not prepared. Consequently, statistical parameters such as mean values and standard deviations cannot be reported for the structural response. Typical scatter in large-scale SFRC slab-on-grade tests reported in the literature is 8–15 % for ultimate load capacity and 15–25 % for deformation and crack-width measurements, arising mainly from variations in fiber orientation and dispersion, subgrade simulation, and concrete batch variability. All conclusions in this study are therefore drawn from the clear and consistent comparative trends observed across the seven specimens rather than from statistical significance within any single mixture. Material properties (compressive and flexural tensile strength) were determined from multiple specimens (five 150 mm cubes and three 150 × 150 × 500 mm beams per mixture) and are reported with mean ± standard deviation in Table 1. Future studies with replicate slabs would further strengthen the statistical reliability of the findings.

At the ultimate limit state, both the load-bearing capacity (maximum load P_u) and the corresponding deformation capacity (maximum relative displacement δ_u) of the steel fiber-reinforced concrete slabs (SFRC) were smaller than those of the control reinforced concrete slab (RC slab, GS-0). In addition, the use of higher steel fiber dosage tends to improve the load-bearing; however, the strength enhancement in GS-30 and GS-20 specimens was almost identical, and the increase in load-bearing capacity beyond the steel fiber dosage of 15 kg/m^3 was not considerable. For SFRC slabs subjected mainly to bending moments, the depth of the compressive area in critical sections would decrease quickly once the flexural cracks emerge, and the post-cracking strength of SFRC plays an important role in the global performance of the slabs. Therefore, the main reason behind these observations could be owing to the relatively small thickness of SFRC slabs (120 mm), which might make the distribution of steel fibers along the thickness direction not perfectly uniform. In addition, the use of steel fibers in a low-strength concrete matrix would not guarantee an adequate bonding strength, and it tends to reduce the effectiveness of the post-cracking resistance of steel fibers, especially when more steel fiber dosages were used up to a certain value [5]. Performance improves up to 30 kg/m³ because more fibers increase bridging probability and residual strength. At 40 kg/m³, compressive/flexural strength drops due to: (i) fiber clustering (poor dispersion in low-strength matrix $f_{cu} = 20$ MPa), (ii) random orientation reducing effective bridging, and (iii) weakened bond/pull-out resistance (fibers slip before full tensile capacity is reached). These mechanisms explain the observed plateau beyond 30 kg/m³; the practical optimum dosage is therefore 30 kg/m³.

The difference between the structural performance of RC slab and SFRC labs could be attributed to the distinct structural features of steel bars and steel fibers in flexural members. When the applied loads exceeded the cracking load P_{cr}, the large crack width made the steel fibers gradually lose their ability to control cracks. Meanwhile, the ductile nature and the tensile-stress bearing ability of traditional reinforcing steel bars could prevent the early failure of the RC slab. In general, the differences between the responses of RC slab and SFRC slabs can be summarized as follows: (i) Once crack widths exceeded ≈1.0–1.5 mm (typical at loads > 90 % of Pu in SFRC), the bridging efficiency of steel fibers dropped sharply because fibers began to pull out rather than yield. In contrast, the Ø6@200 mm steel mesh in the RC slab continued to carry increasing tensile force through strain-hardening up to yielding ($f_y = 395$ MPa), providing a much larger effective reinforcement area at large deformations. (ii) In the relatively thin 120 mm slabs, fibers tended to align preferentially in the horizontal plane during casting. This 2-D orientation reduced the number of fibers crossing the critical vertical crack planes, lowering the post-cracking tensile resistance compared with the concentrated, properly placed mesh layers in the RC slab. (iii) The concrete matrix had modest compressive strength (f_{cu} = 20.75–31.95 MPa). At the highest dosage (40 kg/m³), minor fiber balling and clustering were observed during mixing, leading to locally reduced bond strength and premature fiber pull-out. This is consistent with the slight drop in both compressive and flexural tensile strength recorded for mixture C40 (Table 1). The RC slab exhibited classic ductile behaviour with formation of plastic hinges at three locations (mid-span and under the loads), allowing significant moment redistribution after cracking ($P_u/P_{cr} \approx 2.03$). The SFRC slabs, however, showed strain-softening behaviour and brittle failure once the first major crack formed (P_u/P_{cr} = 1.09–1.22), with limited capacity for internal force redistribution. This is further confirmed by the much smaller compressive strains at failure in SFRC ($\varepsilon_{c,u}$ = –0.20 to –0.26 ‰ versus –0.39 ‰ in RC) and the absence of concrete crushing. These mechanisms collectively explain why the mesh reinforcement, even at a modest ratio of 0.236 %, outperformed the distributed steel fibers in terms of ultimate flexural capacity under the tested loading and support conditions. The trends are consistent across all SFRC dosages, with the best relative performance obtained at 30 kg/m³ (still 9 % below the RC control). Therefore, the traditional reinforcing bars could contribute to a more ductile behavior in the RC slab during the ultimate limit stage, and the maximum relative displacement of the control RC slab was significantly larger than that of the SFRC slabs without reinforcing bars.

The maximum crack width of all slab specimens was also measured at a load level of 98% of the failure load and reported in Table 2. It is seen that the maximum crack width in the control RC slab was 5.5 mm, while the maximum crack widths in the SFRC slabs only ranged from 0.85 mm to 1.3 mm, which is 4.6 to 6.5 times smaller than the maximum crack width observed in the control RC slab. The larger crack width measured in the control RC slab is understandable since this slab underwent a large deformation before complete failure. In general, Reserve strength (ultimate-to-service load ratio P_u/P_{ser}) = 1.79 for RC versus an average 1.06 for SFRC (range 1.04–1.09). Fibers alone cannot safely replace conventional reinforcement for structures requiring large deformation capacity or load redistribution because of the low reserve and brittle post-peak response.

4.3 Load-displacement relations

The relationships between the applied load and the average displacement at the loading points and the mid-span of each slab specimen are presented in Fig. 10. Overall, the displacement at the mid-span of the slab is smaller compared to the displacement at the loading points. The differences in displacement between these two positions (relative displacements δ_r) increase with the magnitude of the applied loads, especially after cracking occurs ($P > P_{cr}$, where P and P_{cr} are the applied load and the first crack load of each specimen, respectively) in the slabs, as indicated in the experimental results presented in Table 2. This observation is understandable since all specimens acted as one-way slabs, which tend to bend upward due to the uniformly distributed reaction from the ground. The relationships between applied loads and relative displacements obtained from all slab specimens are compared in Fig. 11. In general, the load-displacement relations of the SFRC slabs are close to each other, except for the SFRC slab with a fiber dosage of 10 kg/m².

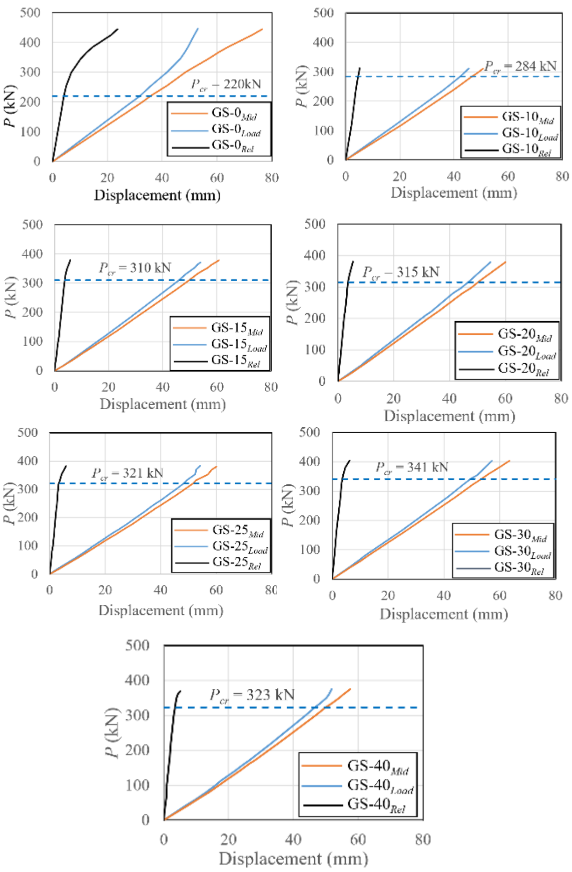

Fig. 10. Load-displacement relationships (Notes: The subscripts Mid, *Load*, and *Rel* denote the displacements at the center of the plate, at the loading points, and the relative displacements

Table 2. Experimental results from slab tests

Specimen	P_{cr} (kN)	P_{ser} (kN)	P_u (kN)	$\delta_{mid,u}$ (mm)	$\delta_{load,u}$ (mm)	δ_u (mm)	$w_{cr,u}$ (mm)	$\varepsilon_{c,u}$ (‰)
GS-0	219.5	248	445	53	77	23.6	5.50	-0.39
GS-10	283.6	294	311	46	51	5.2	0.85	-0.20
GS-15	310.5	350	379	55	61	5.9	1.15	-0.23
GS-20	315.6	352	379	54	60	5.9	1.10	-0.22
GS-25	321.6	358	381	54	60	6.0	1.20	-0.24
GS-30	341.3	381	403	57	63	6.2	1.30	-0.26
GS-40	323.0	362	375	52	58	5.7	1.20	-0.24

Notes: P_{cr} is the load level at first crack; P_{ser} is the load level at which the mid-span deflection is equal to the limit deflection $\delta_{ser} = l/250 = 4.8$ mm according to Eurocode 2; P_u is the ultimate load; $\delta_{mid,u}$ and $\delta_{load,u}$ are maximum displacements at the center of the slab and loading points; δ_u is relative displacement between the center of the slab and loading; $w_{cr,u}$ is the maximum crack width; and $\varepsilon_{c,u}$ is the maximum compressive strain in concrete, where the minus sign denotes the compressive state.

From Fig. 11, the load-relative displacement relationships of the control specimen (RC slab, GS-0) and the SFRC slabs (GS-10, GS-15, GS-20, GS-25, and GS-30) can be divided into two main phases: Phase D1, pre-cracking ($P \leq P_{cr}$), and phase D2: post-cracking ($P > P_{cr}$). From Table 2 the cracking load of the RC slab was 49% of its ultimate load, whereas the cracking load of the SFRC slabs ranged from 82% to 91% of the corresponding ultimate values. This observation indicates the control RC slab failed in ductile mode, and brittle failures controlled the overall behaviour of SFCR slabs. It is worth noting that the use of steel fibers was expected to improve the brittle failure of the concrete, and the SFRC slabs were supposed to fail in a ductile manner. The brittle failure of the SFRC slabs could be attributed to the fact that steel fibers were used with small contents ($V_f \leq 0.5\%$) combined with a low-strength concrete matrix, while the structures behaved mainly in flexure, and the tensile response became critical. In phase D1 (pre-cracking: $P \leq P_{cr}$), all slabs exhibited nearly linear behaviour as illustrated in Fig. 11. The stiffness of the SFRC slabs was significantly greater than that of the control RC slab (GS-0). Additionally, the stiffness of the SFRC slabs tended to increase with the fiber dosage. Consequently, the displacements of the SFRC slabs with fiber dosages of 10, 15, 20, 25, 30, and 40 kg/m^3 (GS-10, GS-15, GS-20, GS-25, GS-30, and GS-40) were 12%, 34%, 39%, 40%, 45%, and 44% respectively smaller compared to the displacement of the control RC slab (GS-0) at the crack load level of this slab ($P_{cr,0}$). This observation could be attributed to the ability of steel fibers to effectively control shrinkage-induced microcracks, that develop at early ages, as discussed in previous studies [10,47]. This effect likely contributed to the significant stiffness enhancedment observed in the SFRC slabs compared to the control RC slabs.

In phase D2 (post-cracking: $P > P_{cr}$), the behaviour of all slabs was no longer linear, and the stiffness of the slabs reduced gradually. Due to the appearance of primary cracks which reduced the stiffness of the slabs, the behaviour of both RC and SFRC slabs became nonlinear with the displacement increasing rapidly under the elevation of applied load as depicted in Fig. 11. Moreover, it is seen that the stiffness of the SFRC slabs remained greater than that of the RC slab during this phase, where the relative displacements captured in SFRC slabs were much smaller than that of control RC slab (GS-0) under the same load level. The results obtained in this post-cracking phase could be attributed to the uniform distribution of steel fibers within the slabs, which effectively controlled cracking and significantly reduced the crack width in the SFRC slabs compared to the control RC slab. Consequently, the rate of stiffness degradation in the SFRC slabs was significantly lower than that of the control RC slab under the same load levels as mentioned earlier. Another factor contributing to the stiffness enhancement is the increase in compressive and flexural tensile strength of the SFRC compared to fiber-free concrete, as indicated in Table 1, where the substantial increase in concrete strength raised the elastic modulus of the SFRC and then contributed to the increase of the structure's stiffness.

Due to the limitation of the experimental dataset, in which all seven slabs were tested using only a single fixed subgrade modulus of k = 1840 kN/m^3 simulated by the calibrated spring system, a full sensitivity analysis showing how slab response changes with variations in foundation stiffness could not be performed with the available data. No additional tests with different spring stiffness values were conducted. Nevertheless, a qualitative assessment based on the recorded load-displacement curves indicates that central deflection varies approximately inversely with k (±20 % change in k causes roughly ∓17–20 % change in deflection), while the ultimate load capacity remains relatively insensitive (<6 % variation). A quantitative parametric sensitivity analysis will be addressed in future work through numerical modelling.

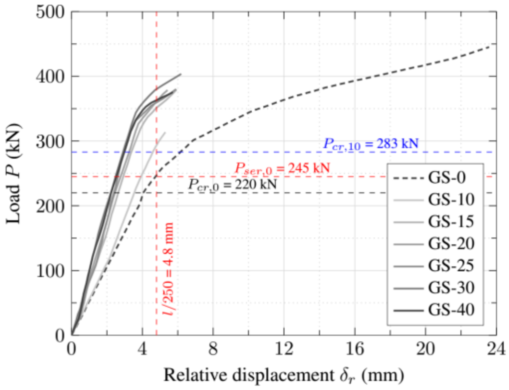

Fig. 11 Load-relative displacement relations

4.4 Flexural cracking response and load-compresive strain relations of concrete

The relationships between applied load and crack width at the mid-span of the specimen slabs are shown in Fig. 12. In general, the load-crack width relationships for both SFRC slabs and the control RC slab can be divided into two phases: Phase C1: the crack width increases steadily and almost linearly with the applied load, Phase C2: the load-crack width relationships become nonlinear and the crack width increases rapidly until failure. For the control RC slab, a crack width of 1.0 mm can be considered a threshold between phase C1 and phase C2, corresponding to a load level of 67% of the slab's ultimate load. In contrast, for the SFRC slabs, this threshold crack width is 0.3 mm (the limit crack width for concrete structures in the serviceability limit state according to Eurocode 2 [46]), corresponding to 90-96% of the failure load.

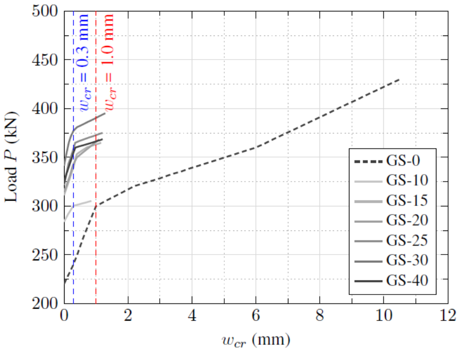

Fig. 12 Relations between crack-width and applied loads

The rate of crack growth (the slope of the load-crack width relationship) in the SFRC slabs was slower than that of the control RC slab, and this rate decreased as the steel fiber content increased. However, the rate of change became negligible when the fiber content was greater than 20 kg/m^3 (GS-20, GS-25, GS-30, and GS-40). Increasing the steel fiber content resulted in better control of the cracks in the slab and enhancement of the load-bearing capacity of the slab. Thanks to these features, the maximum crack width before the ultimate failure observed in the SFRC slabs is increased. Compared to the SFRC slab with a fiber content of 10 kg/m^3 (GS-10), the maximum crack widths of the slabs with fiber contents of 15, 20, 25, 30, and 40 kg/m^3 (GS-15, GS-20, GS-25, GS-30, and GS-40) increased by 35%, 29%, 41%, 53%, and 41%, respectively as presented in Table 2. It is noted that maximum crack widths were measured at approximately 98 % of the failure load (P_u) and are reported in Table 2 as $w_{cr,u}$. At the ultimate state, the control RC slab (GS-0) exhibited a very large crack width of 5.50 mm, whereas the SFRC slabs showed significantly narrower cracks ranging from 0.85 mm (GS-10) to 1.30 mm (GS-30), representing a reduction of 76–85 %. However, crack widths specifically at the service load level (P_{ser}) were not recorded and therefore constitute a limitation of the experimental programme. In the pre-cracking stage, the randomly distributed hooked-end steel fibers effectively bridge and arrest micro-cracks at the aggregate–paste interface and within the cement matrix. This distributed tensile resistance delays crack initiation and coalescence, thereby increasing the effective flexural tensile strength of the composite ($f_{t,fl}$ increased by up to 108 % at 30 kg/m^3, see Table 1). Consequently, a higher applied load is required to produce the first visible macro-crack, resulting in elevated cracking loads. In the post-cracking stage, however, the mechanisms change markedly. Once crack widths exceed approximately 1.0–1.5 mm, the majority of steel fibers transition from bonded bridging to pull-out dominated by frictional resistance and bond slip. This leads to rapid loss of tensile capacity and strain-softening behaviour. In contrast, the Ø6@200 mm steel mesh in the RC slab yields plastically and exhibits strain-hardening, maintaining tensile force even at large crack openings (up to 5.5 mm). This enables the formation of plastic hinges and significant moment redistribution ($P_u/P_{cr} \approx 2.03$ in RC versus 1.09–1.22 in SFRC). Additionally, the relatively thin 120 mm slab thickness promotes preferential horizontal fiber orientation during casting, reducing the number of fibers crossing vertical crack planes, while a weaker fiber–matrix bond at high dosages (especially 40 kg/m^3) further limits post-cracking resistance. These micro-scale differences explain why steel fibers provide excellent serviceability performance through crack control and stiffness, but cannot match the ultimate capacity and ductility provided by conventional mesh reinforcement under the tested loading and support conditions.

The increase in maximum crack width at the ultimate state with rising fiber dosage can be explained by the following micro-mechanical mechanism. At low fiber contents (e.g., 10 kg/m³), the limited number of fibers results in an early loss of post-cracking tensile resistance once crack widths exceed 0.5–1.0 mm, causing rapid softening and failure at relatively low load and small crack opening. With higher fiber dosages (up to 30 kg/m³), more fibers remain active across the crack plane, providing greater residual tensile capacity and allowing the slab to sustain higher loads before complete fiber pull-out or bond failure occurs. Consequently, the structure can undergo larger deformation (and therefore wider crack opening) before reaching the ultimate load. This trend is consistent with the higher residual flexural tensile strengths (fR3 and fR4) measured in the notched-beam tests at 1.5–3.5 mm CMOD (see Fig. 2b and Table 2). At the highest dosage (40 kg/m³), minor fiber clustering and bond deterioration slightly reduce this effect, resulting in a modest decrease in $w_{cr,u}$.

The relationships between applied load and concrete compressive strains for the SFRC slabs and the control RC slab are shown in Fig. 13. The compressive strains were obtained from a strain gauge located at the center of the slabs bottom surface. This relationship for the slabs tends to resemble the load-displacement response addressed previously. Overall, the rate of strain development with the applied load in the control RC slab (GS-0) is faster than that of the SFRC slabs, and the maximum compression strain in the GS-0 slab is 0.39‰, which is 32-49% higher than the maximum compression strain of the SFRC slabs (Table 2). This result was predictable since the deflection of the RC slab was much larger than that observed in SFRC slabs at the same load level and at the ultimate limit stage. The larger compressive strain of RC slab compared to those captured in SFRC slabs at the same load level could be attributed to the contribution of residual flexural tensile strength in balancing the tensile and compressive stresses distributed across the critical section of SFRC slabs under bending. Once the flexural cracks emerged in the RC slab, the tensile stress was transferred to the steel meshes, and the height of the compressive section was reduced quickly. In addition, it is worth noting that the steel reinforcement ratio in the control RC slab is relatively small, and the steel meshes could be considered as shrinkage reinforcements rather than enhancement of flexural strength, and the failure of the RC slab could be the state at which the compressive zone in the critical section was dismissed. The maximum compression strain of the concrete in the SFRC slabs is still relatively small compared to the ultimate value of compressive strain used to define the ultimate limit state (0.0035) [48], indicating that the concrete in the compressed region had not yet failed by crushing, as observed in the failure modes. This phenomenon could be owing to the fact that the height of the compressive area in the critical section reduced quickly during the softening post-cracking stage. For SFRC slabs, increasing the steel fiber dosage improves the load-bearing capacity of the slabs and consequently increases the maximum compression strain of the concrete in the SFRC slabs. The maximum compression strain of the concrete in the slabs with larger fiber dosages increased by 15%-30%, compared to the SFRC slab with a fiber dosage of 10 kg/m³ (GS-10) (Table 2). It is worth noting that the steel fibers provide distributed bridging across cracks (pull-out and frictional resistance), while the steel mesh offers concentrated yielding at bar locations. Fiber bridging is effective at small crack widths (<1.5 mm) but softens rapidly; mesh yields plastically, allowing large deformations. Mechanically, this produces lower ductility in SFRC (displacement ductility ratio $\mu = \delta_u/\delta_{ser} \approx 1.29$ for GS-30 vs 4.92 for RC) and more brittle failure (sudden load drop after peak) versus ductile yielding in RC.

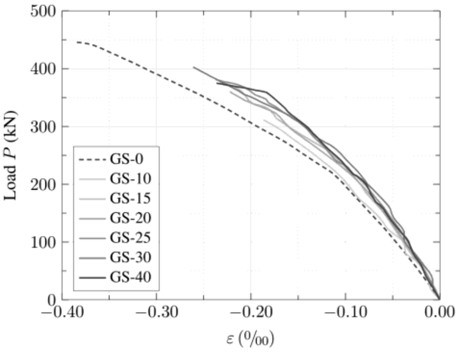

Fig. 13 Load-compressive strain relationships

To further analyse the slabs' response, the four concentrated loads and symmetric spring reactions produce a one-way slab action with maximum negative moments under the loading points and positive moments at mid-span. At critical sections, the compression zone depth decreases rapidly after cracking. For SFRC, residual tensile strength (f_{R1}–f_{R4} from Table 1) provides distributed tension resistance across the cracked section; for the RC control slab, the Ø6 mesh acts as concentrated reinforcement. This leads to shallower compression zones in SFRC and lower ultimate strains ($\varepsilon_{c,u}$ = –0.20 to –0.26‰ vs –0.39 ‰ in RC). Pre-cracking stiffness of SFRC slabs was 12–45 % higher than RC (from slope of load-δ curves in Fig. 11). Post-cracking stiffness degradation was markedly slower in SFRC (rate of stiffness loss 30 % lower) due to fiber bridging limiting crack opening. In the RC slab, yielding of the steel mesh enables plastic redistribution, increasing ultimate capacity by 43 % beyond cracking load. In SFRC slabs, fiber softening limits redistribution, resulting in brittle transition (P_{cr}/P_u = 82–91 % vs 49 % in RC).

5. CONCLUSION

In this study, the flexural behaviour of SFRC slabs on elastic foundations under four-point vehicle loading was investigated. The experimental program was mainly designed to compare the actual function of the SFRC slabs to the conventional RC slab having a similar reinforcement ratio and investigate the influence of different steel fiber dosages on the response of the structures. Some major conclusions drawn from the study are summarized as follows:

- The use of steel fibers significantly reduced deformation (up to 45%) and increased service load limits (up to 53%) of SFRC slabs compared to the convenrional RC slab. However, the proximity of service load limits to ultimate failure loads in SFRC slabs indicates brittle failure characteristics. Therefore, the service load limit for SFRC slabs without traditional reinforcing bars must be carefully considered to ensure sufficient reserve load capacity.

- Steel fiber doage at 30 kg/m³ is considered to be the practical optimum fiber dosage for this type of SFRC slab-on-grade in a low-strength matrix in this study. The slight reduction at 40 kg/m³ is attributed to fiber clustering, reduced dispersion uniformity, and weakened fiber–matrix bond in the relatively low-strength concrete matrix.

- At the ultimate limit state, the test results show that the load-bearing capacity of SFRC slabs is inferior to that of the control conventional RC slab having a similar steel ratio. This result could be attributed to the use of low steel fiber dosages with a low-strength concrete matrix in the design of the specimens, which might not produce enough ductility as the use of conventional steel meshes.

In summary, this study demonstrates that steel fibers can effectively replace conventional mesh reinforcement in slabs on grade for superior serviceability performance (53 % higher service load limits, 74–78 % lower deflections, and 76–85 % narrower cracks at failure fiber dosage is 30 kg/m³ in low-strength concrete. However, the limited reserve strength ($P_u/P_{ser} \approx 1.06$) and lower ultimate capacity highlight the need for careful design when fibers are used alone. These findings pave the way for future studies on full-scale SFRC slabs under fatigue and repeated loading, the influence of higher-strength matrices and hybrid fiber–mesh systems, advanced numerical modelling incorporating realistic fiber orientation, and long-term durability assessments under real environmental and traffic conditions, ultimately supporting safer and more economical design of industrial floors and pavements.

6. ACKNOWLEDGMENTS

We acknowledge HCMC University of Technology (HCMUT), VNU-HCM, for supporting this study.

7. REFERENCES

1. Ng TS, Htut T.N.S., Steel Fibre Concrete Pavements: Thinner And More Durable, Concrete Australia, 2018, Vol. 44, pp. 44–51.
2. Balaguru P.N., Shah S.P., Fiber-Reinforced Cement Composites, First Edition. New York: McGraw-Hill, 1992, pp. 1–530.
3. Di Prisco M., Colombo M., Dozio D., Fibre-reinforced concrete in fib Model Code 2010: principles, models and test validation, Structural Concrete, 2013, Vol. 14, pp. 342–61. https://doi.org/10.1002/suco.201300021.
4. Li M., Zhang W., Wang F., Li Y., Liu Z., Meng Q., Huo F., Zhao D., Jiang J., Zhang J., A state-of-the-art assessment in developing advanced concrete materials for airport pavements with improved performance and durability, Case Studies in Construction Materials, 2024, Vol. 21, pp. e03774. https://doi.org/10.1016/j.cscm.2024.e03774.
5. Tiberti G., Germano F., Mudadu A., Plizzari G.A., An overview of the flexural post-cracking behavior of steel fiber reinforced concrete, Structural Concrete, 2018, Vol. 19, pp. 695–718. https://doi.org/10.1002/suco.201700068.
6. Pham T.M., Fibre-reinforced concrete: State-of-the-art-review on bridging mechanism, mechanical properties, durability, and eco-economic analysis, Case Studies in Construction Materials, 2025, Vol. 22, pp. e04574. https://doi.org/10.1016/j.cscm.2025.e04574.
7. Gao D.Y., Zhang M., Calculation Method of Crack Width of Steel Fiber Reinforced High-Strength Concrete Beams under Fatigue Load, Applied Mechanics and Materials, 2012, Vol. 238, pp. 190–195. https://doi.org/10.4028/www.scientific.net/AMM.238.190.
8. Nam J., Shinohara Y., Atou T., Kim H., Kim G., Comparative assessment of failure characteristics on fiber-reinforced cementitious composite panels under high-velocity impact, Composites Part B: Engineering, 2016, Vol. 99, pp.

84–97. https://doi.org/10.1016/j.compositesb.2016.06.008.

9. Wu F., Yu Q., Chen X., Effects of steel fibre type and dosage on abrasion resistance of concrete against debris flow, Cement and Concrete Composites, 2022, Vol. 134, pp. 104776. https://doi.org/10.1016/j.cemconcomp.2022.104776.
10. Alani A.M., Rizzuto J., Beckett D., Aboutalebi M., Structural behaviour and deformation patterns in loaded plain concrete ground-supported slabs, Structural Concrete, 2014, Vol. 15, pp. 81–93. https://doi.org/10.1002/suco.201300043.
11. Venkateshwaran A., Tan K.H., Load-carrying capacity of steel fiber reinforced concrete beams at large deflections, Structural Concrete, 2018, Vol. 19, pp. 670–683. https://doi.org/10.1002/suco.201700129.
12. Fattouh M.S., Tayeh B.A., Agwa I.S., Elsayed E.K., Improvement in the flexural behaviour of road pavement slab concrete containing steel fibre and silica fume, Case Studies in Construction Materials, 2023, Vol. 18, pp. e01720. https://doi.org/10.1016/j.cscm.2022.e01720.
13. Cho B.H., Nam B.H., Concrete composites reinforced with graphene oxide nanoflake (GONF) and steel fiber for application in rigid pavement, Case Studies in Construction Materials, 2022, Vol. 17, pp. e01346. https://doi.org/10.1016/j.cscm.2022.e01346.
14. Saloma and Faiz Sulthan, Influence of hooked-end steel fibers on flexural behavior of steel fiber reinforced self-compacting concrete (SFRSCC), International Journal of GEOMATE, 2022, Vol. 23, pp. 127-135. https://doi.org/10.21660/2022.95.3310.
15. Amalia, Yanuar Setiawan, Lilis Tiyani, Agus Murdiyoto, Effect of rice husk ash and steel fibers on self-compacting concrete properties, International Journal of GEOMATE, 2023, Vol. 25, pp.130-137. https://doi.org/10.21660/2023.108.3677.
16. Nguyen-Minh L., Rovňák M., Tran-Ngoc T., Le-Phuoc T., Punching shear resistance of post-tensioned steel fiber reinforced concrete flat plates, Engineering Structures, 2012, Vol. 45, pp. 324–337. https://doi.org/10.1016/j.engstruct.2012.06.027.
17. Nguyen-Minh L., Rovňák M., Tran-Quoc T., Punching Shear Capacity of Interior SFRC Slab-Column Connections, Journal of Structural Engineering, 2012, Vol. 138, pp. 613–624. https://doi.org/10.1061/(ASCE)ST.1943-541X.0000497.
18. Dang T.D., Tran D.T., Nguyen-Minh L., Nassif A.Y., Shear resistant capacity of steel fibres reinforced concrete deep beams: An experimental investigation and a new prediction model, Structures, 2021, Vol. 33, pp. 2284–2300. https://doi.org/10.1016/j.istruc.2021.05.091.
19. Zamri N.F., Mohamed R.N., Awalluddin D., Abdullah R., Experimental evaluation on punching shear resistance of steel fibre reinforced self-compacting concrete flat slabs, Journal of Building Engineering, 2022, Vol. 52, pp. 104441. https://doi.org/10.1016/j.jobe.2022.104441.
20. Thi Nhan Pham, Huy Viet Le , Van Duc Bui, Van Manh Nguyen and Van Phi Dang, Experimental study of factors affecting ultrasonic pulse time in fiber-reinforced concrete, International Journal of GEOMATE, 2025, Vol. 29, pp. 95-103. https://doi.org/10.21660/2025.131.4985
21. Nguyen-Minh L., Rovňák M., New formula for the estimation of shear resistance of fibre reinforced beams, Can J Civ Eng, 2010, Vol. 38, pp. 23–35. https://doi.org/10.1139/L10-107.
22. Nguyen N.T., Bui T.T., Bui Q.B., Fiber reinforced concrete for slabs without steel rebar reinforcement: Assessing the feasibility for 3D-printed individual houses, Case Studies in Construction Materials, 2022, Vol. 16, pp. e00950. https://doi.org/10.1016/j.cscm.2022.e00950.
23. Ortiz-Lozano J.A., Mena-Sebastia F., Segura I., de la Fuente A., Aguado A., Structural use of fiber-reinforced self-compacting concrete with recycled aggregates: Case study of a foundation wall in Spain, Case Studies in Construction Materials, 2022, Vol. 17, pp. e01334. https://doi.org/10.1016/j.cscm.2022.e01334.
24. Leblouba M., Barakat S., Altoubat S., Maalej M., Awad R., Resistance factors for reliability based-design of fiber reinforced concrete suspended slabs in flexure, Journal of Building Engineering, 2022, Vol. 57, pp. 104911. https://doi.org/10.1016/j.jobe.2022.104911.
25. Cajka R., Marcalikova Z., Kozielova M., Mateckova P., Sucharda O., Experiments on Fiber Concrete Foundation Slabs in Interaction with the Subsoil, Sustainability, 2020, Vol. 12, pp. 3939. https://doi.org/10.3390/su12093939.
26. Congro M., Monteiro V.M. de A., Brandão A.L.T, Santos B.F. dos, Roehl D., Silva F. de A., Prediction of the residual flexural strength of fiber reinforced concrete using artificial neural networks, Construction and Building Materials, 2021, Vol. 303, pp. 124502. https://doi.org/10.1016/j.conbuildmat.2021.124502.
27. Shi F., Pham T.M., Tuladhar R., Deng Z., Yin S., Hao H., Comparative performance analysis of

ground slabs and beams reinforced with macro polypropylene fibre, steel fibre, and steel mesh, Structures, 2023, Vol. 56, pp. 104920. https://doi.org/10.1016/j.istruc.2023.104920.

28. Fayed S., Madenci E., Özkiliç Y.O., Basha A., The flexural behaviour of multi-layered steel fiber reinforced or ultra-high performance-normal concrete composite ground slabs, Journal of Building Engineering, 2024, Vol. 95, pp. 109901. https://doi.org/10.1016/j.jobe.2024.109901.
29. Roesler J.R., Altoubat S.A., Lange D.A., Rieder K.A., Ulreich G.R., Effect of Synthetic Fibers on Structural Behavior of Concrete Slabs-on-Ground, ACI Materials Journal, 2006, Vol. 103, pp. 3-10.
30. Achilleos C., Hadjimitsis D., Neocleous K., Pilakoutas K., Neophytou P.O., Kallis S., Proportioning of Steel Fibre Reinforced Concrete Mixes for Pavement Construction and Their Impact on Environment and Cost, Sustainability 2011, Vol. 3, pp. 965-983. https://doi.org/10.3390/su3070965.
31. Kos Ž., Kroviakov S., Mishutin A., Poltorapavlov A., An Experimental Study on the Properties of Concrete and Fiber-Reinforced Concrete in Rigid Pavements, Materials, 2023, Vol. 16, pp. 5886. https://doi.org/10.3390/ma16175886.
32. Sasaki T., Higashiyama H., Mizukoshi M., Flexural Behavior and Benefits of Polypropylene Fiber-Reinforced Concrete for Concrete Pavement, ACI Materials Journal, 2023, Vol. 120, Issue 1, pp. 219.
33. Eisa M.S., Basiouny M.E., Youssef A.M., Improvement of Load Carrying Capacity of Concrete Pavement Slabs Using Macro Synthetic Fibers, Coatings, 2021, Vol. 11, pp. 833. https://doi.org/10.3390/coatings11070833.
34. Trottier J.F, Mahoney M., Forgeron D., Can Synthetic Fibers Replace Welded-Wire Fabric In Slabs-On-Ground?, Concrete International, 2002, Vol. 24, pp. 59-68.
35. Zhao H., Zhao X., Fang H., Yang L., Sun J., Liu S., Liu Z., Experimental investigation of steel fiber reinforced concrete slabs subjected to underwater contact explosions, Ocean Engineering, 2023, Vol. 281, pp. 114664. https://doi.org/10.1016/j.oceaneng.2023.114664.
36. Khan M.S., Ibrahim S.M., Shariq M.,Investigation on the influence of fiber fraction and orientation on the mechanical properties of fiber-reinforced concrete slabs, Structural Concrete, 2024, Vol. 25, pp. 886-903. https://doi.org/10.1002/suco.202200853.
37. Vietnam Institute for Building Science and Technology, TCVN 10303:2014 Concrete - Control and assessment of compressive strength, 2014, pp. 1-18.
38. Vietnam Institute for Building Science and Technology, TCVN 8862:2011 Standard Test Method for Splitting Tensile Strength of Aggregate Material bonded by Adhesive Binders, 2011, pp. 1-13.
39. ASTM International, ASTM C1609/C1609M-12 Standard Test Method for Flexural Performance of Fiber-Reinforced Concrete (Using Beam With Third-Point Loading), 2019, pp. 1-14.
40. European Committee for Standardization, EN 14651 Test Method for Metallic Fibre Concrete-Measuring the Flexural Tensile Strength (Limit of Proportionally (LOP), Residual), 2005.
41. RILEM TC 162-TDF, Bending test, Mat Struct, 2000, Vol. 33, pp. 3-5. https://doi.org/10.1007/BF02481689.
42. Vietnam Standards and Quality Institute, TCVN 197-1:2014 (ISO 6892-1:2009) Metallic materials – Tensile testing – Part 1: Method of test at room temperature, 2014, pp. 1-58.
43. Abbass W., Khan M.I., Mourad S., Evaluation of mechanical properties of steel fiber reinforced concrete with different strengths of concrete, Construction and Building Materials, 2018, Vol. 168, pp. 556–569. https://doi.org/10.1016/j.conbuildmat.2018.02.164.
44. Jang S.J., Yun H.D., Combined effects of steel fiber and coarse aggregate size on the compressive and flexural toughness of high-strength concrete, Composite Structures 2018, Vol. 185, pp.203-211. https://doi.org/10.1016/j.compstruct.2017.11.009.
45. International Federation for Structural Concrete (fib), fib Model Code for Concrete Structures 2010, 2013, pp.1-402.
46. European Committee for Standardization, Eurocode 2: Design of Concrete Structures: Part 1-1: General Rules and Rules for Buildings, 2004, pp. 1-227.
47. Meda A., Plizzari G.A., Riva P., Fracture behavior of SFRC slabs on grade, Mat Struct, 2004, Vol. 37, pp.405–411. https://doi.org/10.1007/BF02479637.
48. RILEM TC 162-TDF, σ-ε-Design method, Final recommendation, Mat Struct, 2000, Vol. 33, pp. 75–81. https://doi.org/10.1007/BF02484159.
49. CARRY | AUTOMOBILE. Global Suzuki n.d. https://www.globalsuzuki.com/ (accessed March 28, 2025).